



Cite this: DOI: 10.1039/d6ta01545j

Few-layer MoS₂ dispersion induced by sulfur atom sharing to promote CO₂ hydrogenation to methanol†

Gustavo A. S. Alves,^a Silvio Bellomi,^a Tobias Wagner,^a Alberto Tampieri,^a Christian Etzlstorfer,^a Michael Stöger-Pollach,^b Daniel C. Cano-Blanco^{cd} and Karin Föttinger^{id}*^a

With the ongoing interest in developing more stable and versatile catalysts for CO₂ hydrogenation to methanol, molybdenum sulfide (MoS₂) has been recently proposed as an alternative material. However, in its bulk state, CO₂ hydrogenation over MoS₂ typically favors methane formation. In this work, a wet impregnation method is applied for the production of ZnS-supported MoS₂, as confirmed by characterization via X-ray Diffraction, Raman and X-ray Photoelectron Spectroscopy. In contrast with the negligible methanol production shown by the pure MoS₂ reference, 2% MoS₂/ZnS presents a methanol selectivity of 78% at a CO₂ conversion of 2.3% under the mild reaction conditions of 200 °C and 20 bar. Density Functional Theory and Transmission Electron Microscopy suggest that the improved catalytic activity arises from an even dispersion of few-layer MoS₂ with exposed basal plane sites at the ZnS surface, an arrangement possibly enabled by the structural similarity and the shared S atoms between 2H-MoS₂ and W-ZnS phases. This hypothesis is strengthened by the comparison with the reference sample consisting of ZrO₂-supported MoS₂ sample, in which more agglomerated MoS₂ particles resulted in a lower and less selective methanol production. Moreover, *in situ* X-ray absorption spectroscopy and H₂ temperature-programmed reduction suggest further evidence of a MoS₂/ZnS interaction during the H₂ pretreatment, which may promote not only the expected formation of S-vacancies but also a partial reconstruction of MoS₂ given the close contact and sharing of S atoms with the ZnS support.

Received 20th February 2026

Accepted 1st June 2026

DOI: 10.1039/d6ta01545j

rsc.li/materials-a

Introduction

With the growing necessity of phasing out fossil fuels due to the concerning scenario of anthropogenic climate change, the introduction of alternative feedstocks for producing methanol could represent a significant step for a greener chemical industry, as the conventional production of this compound is currently responsible for about 10% of the total CO₂ emissions in this growing sector.¹ In this context, catalytic CO₂ hydrogenation to methanol² may play a key role in the near future, given the possibility of utilizing CO₂ captured from air and a variety of point sources.³ Although Cu/ZnO/Al₂O₃ catalysts are considered the most well-known and established catalyst for this

application,⁴ recent research suggests that alternative formulations including molybdenum sulfide (MoS₂) may present comparable or even higher catalytic performance under similar reaction conditions.⁵ In contrast with Cu-based materials, the non-metallic nature of such catalysts may offer advantages in terms of stability and tolerance to sulfur impurities,⁶ which could benefit processes based on sulfur-rich CO₂ from biogenic sources, for instance.⁷

In addition to CO₂ hydrogenation, MoS₂ has been already implemented as a catalyst for hydrodesulfurization⁸ and more recently researched as a photocatalyst⁹ or electrocatalyst¹⁰ for hydrogen production. Considering the layered structure of MoS₂, these applications have been strongly associated with the reactivity of sulfur vacancies located at edge sites, while basal planes have been generally regarded as an inactive region.¹¹ Similarly, in the context of CO₂ conversion, MoS₂ morphologies with abundant edges are correlated with a high activity for methane production.¹² However, fewer edges and more extensive basal planes can discernibly shift the catalytic activity to favor the production of methanol instead of methane. For this reason, the most MoS₂-based catalysts for CO₂ hydrogenation reported up to date involve few-layer or single-layer MoS₂, in which basal plane S-vacancies are considered the active site for

^aInstitute of Materials Chemistry, TU Wien, Getreidemarkt 9/BC/01, 1060 Vienna, Austria. E-mail: karin.foettinger@tuwien.ac.at

^bUniversity Service Center for Transmission Electron Microscopy (USTEM), TU Wien, Stadionallee 2/057-02, 1020 Vienna, Austria

^cPaul Scherrer Institute, PSI Center for Energy and Environmental Sciences, Villigen PSI, CH-5232, Switzerland

^dÉcole Polytechnique Fédérale de Lausanne (EPFL), Institute of Chemical and Bioengineering, Lausanne CH-1015, Switzerland

† This work is dedicated to Professor Ulrich Schubert on the occasion of his 80th birthday, in honor of his outstanding contributions and inspiring mentorship.



methanol formation through a CO-based pathway.^{5,13} In a different manner, the introduction of other compounds in the MoS₂ synthesis was also shown to be beneficial for methanol selectivity, as observed for ZnS¹⁴ as well as Na-,¹⁵ C-,¹⁶ Cu-,¹⁷ Ni-,¹⁸ Co-¹⁹ and Mn-based²⁰ additives. While some of these promoters directly influence catalytic activity by tuning the content of S-vacancies and providing new sites for H₂ activation, others exert an effect on the morphology of MoS₂ in manner to prevent agglomeration and exposure of edge sites. As an example of the latter, the growth of MoS₂ in spatial confinement with ZnS derived from a metal-organic framework was shown to create hollow composite nanocubes containing MoS₂ with abundant basal-plane S-vacancies and high activity for CO₂ hydrogenation to methanol.¹⁴

In this work, a facile wet impregnation method is applied to produce ZnS-supported MoS₂. In comparison with bulk MoS₂, the material shows superior catalytic performance for CO₂ hydrogenation to methanol, as the strong interaction between the sulfides may inhibit agglomeration and promote the dispersion of few-layer MoS₂ at the surface of the ZnS support.

Experimental

Catalyst synthesis

The synthesis precursor ammonium tetrathiomolybdate (ATTM) was obtained through a procedure similar to a previous report,²¹ in which H₂S was bubbled into a mixture containing 80 g Na₂MoO₄·2H₂O (Carl Roth, 99.5%) diluted in a concentrated ammonia aqueous solution. After about 30 minutes the mixture was cooled in an ice bath for the formation of a precipitate, which was later filtered and dried at room temperature.

ZnS-supported MoS₂ has been synthesized by impregnating powder ZnS (Carl Roth, 99%) with an aqueous solution of ATTM. Initially, 2.5 g of ZnS are mixed with 50 mL H₂O and the appropriate amount of ATTM according to the planned molar concentration of Mo (2 to 10% Mo) in the powder sample. Subsequently, the mixture is transferred to a rotary evaporator where it is dried at approximately 20 mbar. In a tubular furnace under N₂ flow and a heating rate of 10 °C min⁻¹, the solid is further dried at 120 °C for 1 h and finally thermally treated at 400 °C for 2.5 h. For comparison, bulk MoS₂ was produced by thermal treatment of ATTM at the same conditions. Furthermore, ZrO₂-supported MoS₂ and C-supported MoS₂ were obtained by an analogous method using ZrO₂ powder (Fluka, 99%) or Carbon black (Printex XE 2 B, 99%) instead of ZnS.

Characterization

The material has been analyzed by X-ray diffraction (XRD) in a Philips X'Pert diffractometer at 45 kV with a Cu K α source, together with the Crystallography Open Database (COD)²² for further data interpretation. Furthermore, Raman spectroscopy was performed with a Bruker RAMANtouch microscope at 0.2 mW under excitation of a 532 nm laser. For the investigation of surface composition, X-ray Photoelectron Spectroscopy (XPS) was performed in a SPECS μ -Focus system (AlK α source,

Phoibos 150 WAL detector). For XPS data analysis, the CasaXPS software²³ was utilized and the C 1s peak related to adventitious carbon has been fixed at 284.8 eV for calibration of all spectra. Textural properties of the material were analyzed by N₂ physisorption with a Micromeritics ASAP 2020, considering the Brunauer-Emmett-Teller (BET) method for surface area determination. The morphology of the samples was evaluated by Scanning Electron Microscopy (SEM) using a FEI Quanta 250FEG at 5 kV. Further structural features were analyzed by Transmission Electron Microscopy (TEM) with a FEI Tecnai F20 at an accelerating voltage of 200 kV.

In situ X-ray Absorption Spectroscopy (XAS) was performed at the B18 beamline of the Diamond Light Source. The experiments were conducted with powder samples mixed with boron nitride in a quartz capillary at 10 bar pressure and a total flow of 20 mL min⁻¹. After purging with He, the cell was pressurized and heated at a 10 °C min⁻¹ rate under H₂ flow (10% H₂ diluted in He) in order to simulate the catalyst pretreatment conditions at 300 °C during 1 h. Subsequently, the temperature was lowered to 200 °C and CO₂ hydrogenation conditions were simulated by introducing CO₂ in a 1CO₂ : 3H₂ ratio during 1 h, before cooling to room temperature. Mo K-edge XANES spectra were collected in transmission geometry, while gases released during the experiment were analyzed with a Pfeiffer OmniStar Mass Spectrometer. Processing and fitting of EXAFS data were performed using the Demeter software suite²⁴ using *k* values between 3 and 9 and maintaining ΔR lower than 0.02 Å. Temperature-programmed reduction under H₂ (H₂-TPR) was performed with a Microtrac Belcat II, in which 80 mg of catalyst were pretreated under Ar flow at 300 °C, followed by cooling and heating 10 °C min⁻¹ in a 5% H₂ flow, while the outgas was measured by a Thermal Conductivity Detector (TCD). For Temperature-Programmed Desorption of H₂ (H₂-TPD) experiments, 70 mg of catalyst were pretreated at 300 °C under H₂ atmosphere near atmospheric pressure, followed by cooling, evacuation to 0.01 mbar and heating at 10 °C min⁻¹ while the desorbed gas was analyzed by a Pfeiffer OmniStar Mass Spectrometer. An analogous experiment was performed for CO₂-TPD with the addition of a CO₂ dosing step at 50 mbar for 15 minutes before evacuation to 0.01 mbar and heating.

Catalyst testing

The catalytic activity of the samples was evaluated in the tubular fixed-bed reactor PID Effi from Micromeritics, under 1.25 mL_n-min⁻¹ CO₂ + 3.75 mL_n min⁻¹ H₂ flow at 200 °C and 20 bar pressure. Shortly before reaction, a pretreatment with 5 mL_n-min⁻¹ H₂ at 300 °C was performed for catalyst activation. The comparison of different MoS₂ loadings was done with 1 g of catalyst and reaction products were detected in the gas phase with an Inficon Micro GC 3000 equipped with a Plot Q column and a TCD detector. Furthermore, experiments at higher Gas Hourly Space Velocity (GHSV) were performed with 0.5 g_{cat} and 0.25 g_{cat} using an Agilent 7890 GC with FID detection. For the comparison between 2% MoS₂/ZnS and 2% MoS₂/ZrO₂, 0.25 g of sample was diluted with quartz sand to keep the catalyst bed volume constant. Except for the 165 h-long experiment, the



reported product yields refer to approximately 18 h of time on stream.

Density functional theory (DFT) simulation

DFT simulations were performed using the Vienna *Ab Initio* Simulation Package (VASP), version 6.3.²⁵ The Perdew–Burke–Ernzerhof (PBE) generalized gradient approximation was employed using a plane-wave cutoff of 400 eV,²⁶ and including non-spherical contributions of the gradient of density in the PAW spheres.^{27,28} The electronic convergence was eased using 0.05 eV width of Gaussian smearing. All the calculations included the long-range dispersion corrections as implemented in the zero-damping DFT-D3 approach.²⁹ Following previous reports, ZnS was modelled with a reconstructed non-polar (100) termination composed of five layers, each of 12 Zn and 12 S atoms, generated from a cut of the bulk wurtzite structure (COD-ID 1011195). The two bottom layers were kept frozen in the bulk configuration during the optimization, while the uppermost three layers were allowed to relax.³⁰ The ZrO₂ surface was generated starting from the bulk monoclinic reference (COD-ID 1522143), and simulated using a (111) termination according to the literature. The slab was composed of four O–Zr–O tri-layers (each containing 16 Zr and 32 O atoms) of which only the two uppermost were allowed to relax during optimization.³¹ The interface of MoS₂ with the supports was modelled using an Mo₃S₆ patch sliced from an ideal monolayer, including also a configuration with a missing S atom to explicitly describe the Mo–S under-coordination, which was let free to relax in all simulations. The choice of the Mo₃S₆ patch was motivated by the lattice mismatch between the MoS₂ monolayer, ZnS (100), and ZrO₂(111), which would require substantial artificial strain or prohibitively large supercells to construct coherent periodic overlayers (details in Table S1). The finite patch model therefore provides a computationally tractable and physically relevant approach to capture the local edge-mediated interactions, sulfur vacancy formation, and interfacial sulfur sharing. The initial magnetic moments were set as +1.0 μB for Mo, while all other atoms were initialized using 0 μB guesses. For all the models, 15 Å of vacuum were placed along the z-axis to avoid spurious period interactions. The relaxations were performed using a *Γ*-centered 2 × 2 × 1 Monkhorst–Pack grids,³² using thresholds for electronic energies and ionic forces of 10^{−5} eV and 0.05 eV Å^{−1}, respectively. To improve the description of the electronic structure and obtain accurate energies, a finer 5 × 5 × 1 grid was used. The center of an occupied electronic band (*i*) was calculated from the projected density of states (PDOS) using the following equation, where $\varepsilon D_i(\varepsilon)$ is the PDOS of the *i* orbitals weighted by the energy, E_F is the Fermi level, and E_0 is the lower bound of the energy interval.

$$\varepsilon_i = \frac{\int_{E_0}^{E_F} \varepsilon D_i(\varepsilon) d\varepsilon}{\int_{E_0}^{E_F} D_i(\varepsilon) d\varepsilon} \quad (1)$$

To quantify the similarity between two distinct PDOS *i* and *j*, the Tanimoto coefficient (T_C),^{33,34} was used as defined in the following equation. T_C can be interpreted as the overlap between the areas spanned by the PDOS, and takes real values in the range [0,1], being equal to 0 (1) if the functions have no overlap (are identical).

$$T_C(f_i, f_j) = \frac{f_i \times f_j}{|f_i|^2 + |f_j|^2 - f_i \times f_j} \quad (2)$$

The thermodynamic penalty (ΔE_v) for the introduction of a S vacancy in MoS₂ was calculated for each support (S) using the following equation, as the energy difference between the most stable adsorption configurations of the pristine and defective patches, normalized by the number of MoS₂ unit formula ($n_{\text{MoS}_2} = 3$).

$$\Delta E_v = \frac{\text{MoS}_{2-x} - \text{MoS}_2}{\text{support}} \frac{\text{MoS}_2}{n_{\text{MoS}_2}} \quad (3)$$

Results and discussion

Bulk MoS₂ and ZnS-supported MoS₂ have been produced using the same procedure, ATTM as precursor and 400 °C annealing in inert atmosphere. In accordance with previous reports, bulk MoS₂ produced by such a method consists of 2H-MoS₂ (COD-ID 1010993) with low crystallinity, as evidenced by the wide XRD pattern in Fig. 1. The material presents a slab-like morphology with particle length varying from approximately 50 to 150 μm long, in addition to a N₂ adsorption–desorption isotherm indicating mesoporous character with a BET surface area of about 35 m² g^{−1}, as shown by Fig. S1 and S2. After wet impregnation of ZnS with ATTM followed by thermal treatment, XRD confirms the formation of a similar 2H-MoS₂ phase for the

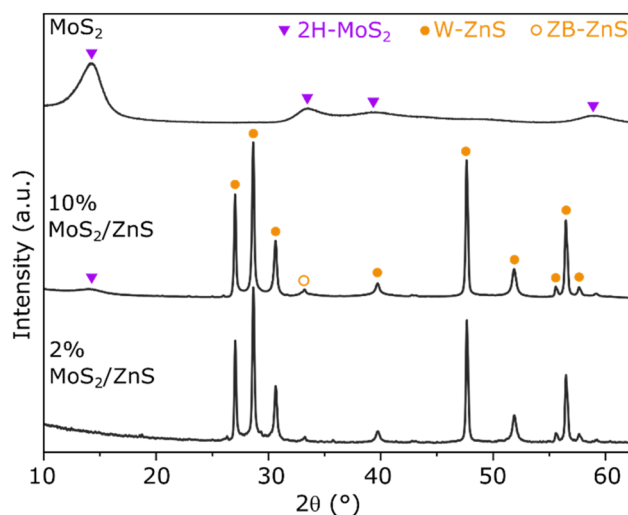


Fig. 1 XRD patterns of bulk MoS₂ and ZnS-supported MoS₂ at 2% and 10% loading.



sample with 10% loading due the signal around 14°, the most intense reflection of bulk 2H-MoS₂ attributed to the interlayer spacing of (002) planes. The remaining features are less intense and cannot be distinguished due to the relatively low loading and crystallinity of MoS₂. In agreement, Fig. S3 shows that no features from 2H-MoS₂ can be distinguished upon impregnation of ZnS with the lower loadings of 5%, 2% and 1%. In all samples containing the ZnS support, its XRD pattern consists of the hexagonal Wurtzite phase (W-ZnS, COD-ID 1011195) with a minor contribution of zinc blende (ZB-ZnS, COD-ID 1100043). Furthermore, no significant shifts and width changes are observed when comparing pure ZnS and the impregnated material in Fig. S3, which indicates that the crystalline structure of the support remains stable upon impregnation and thermal treatment.

The catalytic activity of MoS₂ and ZnS-supported MoS₂ has been evaluated in a fixed bed reactor at 20 bar and 200 °C after a H₂ pretreatment at 300 °C, previously suggested to optimally promote the activation of few-layer MoS₂ catalysts through the formation of S-vacancies.^{5,13} Under these conditions, Fig. 2A shows that bulk MoS₂ presents negligible methanol formation, as its total CO₂ conversion of 7.3% corresponds mostly to CH₄ with CO as a minor product. With the impregnation of 10% MoS₂ on ZnS, the total CO₂ conversion is sharply decreased to 2.9% while the high selectivity towards CH₄ is maintained. This trend suggests that the catalytically active phase in 10% MoS₂/ZnS may still be similar to bulk MoS₂, coherently with the presence of agglomerated MoS₂ with abundant edge S-vacancies, known to promote CO₂ hydrogenation to methane.⁵ However, at lower MoS₂ loadings a distinct trend is observed as the CH₄ yield progressively decreases and CO₂ hydrogenation to methanol becomes considerably more prominent with the selectivity of 46, 78 and 64% while comparable CO₂ conversions

of 3.2, 2.3 and 2.3% are maintained upon the MoS₂ loadings of 5, 2 and 1%, respectively. The favorable catalytic activity at low MoS₂ loading suggests a synergistic interaction between MoS₂ and the support, given that pure ZnS presents negligible activity for CO₂ hydrogenation.¹⁴ For further insights on the kinetic performance of 2% MoS₂/ZnS, catalytic testing has been conducted in a 165 h-long experiment at varying temperatures, complemented by a comparison of different GHSV values as shown in Fig. S4 and S5, respectively. As summarized in Fig. 2B, lower reaction temperatures promote higher CH₃OH selectivity at the expense of lower CO₂ conversions. In fact, between 160 °C and 240 °C, selectivity to methanol drops from 95 to 47% while total CO₂ conversion increases from 0.8 to 3.3%. Interestingly, returning to the reaction temperature of 200 °C after the 240 °C step leads to methanol yields approximately 50% higher than the initial values, while CO and CH₄ production rates remain similar, as shown in Fig. S4. Such an improvement could be associated to extensive formation of surface S-vacancies due to the long reaction time, as suggested by previous studies on other MoS₂-based catalysts,^{5,13,15} although the 240 °C step may play a role on accelerating such process. In view of the promising catalytic activity of 2% MoS₂/ZnS at the mild reaction conditions of 20 bar and 200 °C, the as-synthesized material was further characterized, seeking to better understand the nature of its active phase and role of the H₂ pretreatment on the catalyst structure.

As the low content of the active phase in 2% MoS₂/ZnS prevents clear detection *via* XRD, Raman spectroscopy has been

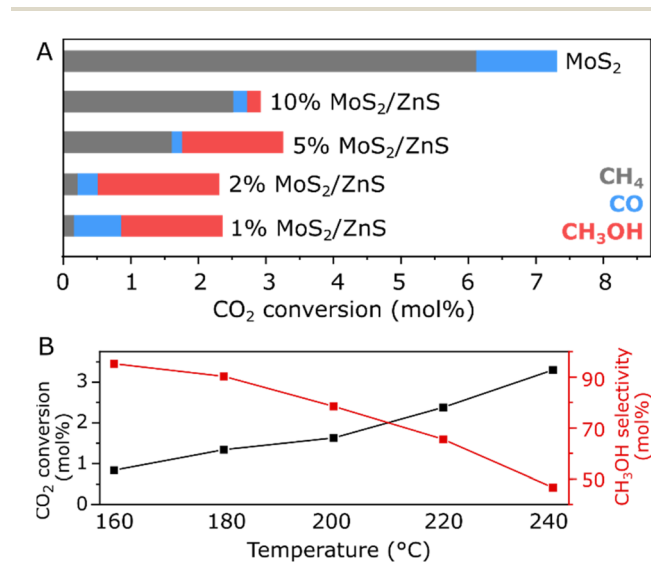


Fig. 2 Catalytic activity of bulk MoS₂ and ZnS-supported MoS₂ in a fixed-bed reactor at 20 bar/200 °C/1 g_{cat} in terms of CO₂ conversion to CH₄, CO and CH₃OH (A) and catalytic activity of 2% MoS₂/ZnS at 20 bar/0.5 g_{cat} in terms of total CO₂ conversion and selectivity to CH₃OH at varied temperatures (B).

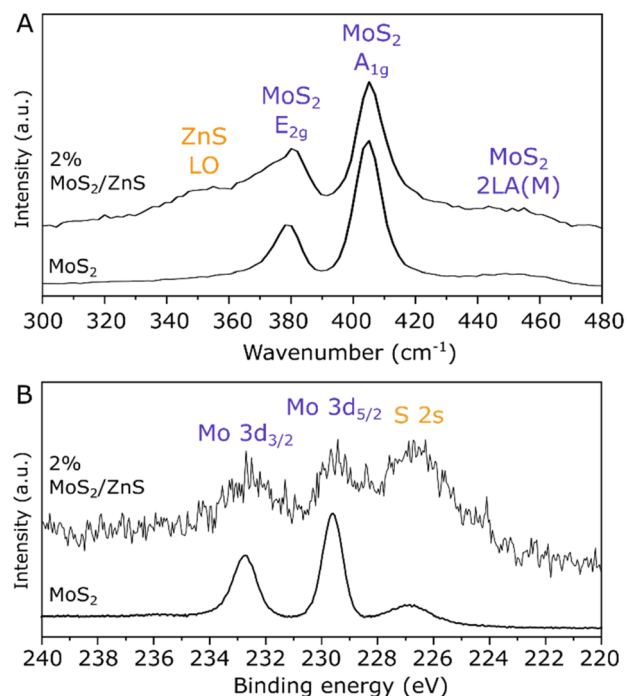


Fig. 3 Raman spectrum with 532 nm excitation (A) and high-resolution XPS spectrum of the Mo 3d/S 2s region (B) of pure MoS₂ and 2% MoS₂/ZnS.



employed, given its sensitivity to detect vibrational modes of layered structures from monolayer to multilayer stacking.³⁵

Accordingly, the spectrum of 2% MoS₂/ZnS in Fig. 3A contains the LO mode from ZnS at 351 cm⁻¹ (ref. 36) in addition to bands related to E_{2g}, A_{1g} and 2LA modes from MoS₂ at 380, 405 and 453 cm⁻¹,³⁵ respectively. As an indicator of MoS₂ layer stacking, a difference of 25 ± 2 cm⁻¹ is observed between E_{2g} and A_{1g} in both samples, consistently with stacking of at least 4 layers.³⁵ Furthermore, analysis of the catalyst surface by XPS in Fig. 3B provides additional evidence for Mo species, as the Mo 3d doublet can be clearly distinguished from the S 2s peak at 226.5 eV, considering the characteristic doublet separation of 3.1 eV.³⁷ While 2% MoS₂/ZnS presents a low-intensity Mo 3d doublet with respect to the S 2s feature due to its low Mo surface content, Fig. S6 shows that the material loaded with 10% MoS₂ has a similar XPS profile to that of pure MoS₂, coherently with the higher prominence of MoS₂ in the XRD pattern of this sample. Importantly, in all cases the presence of MoS₂ at the catalyst surface is consistent with the binding energy of Mo 3d_{5/2} at 229.6 eV, which indicates a Mo⁴⁺ oxidation state and rules out surface oxidation of the sulfide in contact with air due to the absence of Mo⁶⁺ species.^{37,38}

Although Raman and XPS confirm the impregnation of MoS₂ on ZnS, the SEM micrographs of the pristine support and the one impregnated with 2% MoS₂ in Fig. 4A and B present an identical morphology, consisting of similarly rounded particles with smooth surfaces and approximately 100 to 400 nm in size. This agrees with the high dispersion observed from XRD and the homogenous stacking of few layers confirmed by Raman. Accordingly, the material impregnated with 10% MoS₂ shows clearly segregated particles much larger than those attributed to ZnS, as additional evidence for bulk MoS₂ upon such a high catalyst loading. As shown in Fig. S2, the negligible porosity of the ZnS support is maintained after MoS₂ impregnation while its surface area decreases from 9.3 to 6.7 m² g⁻¹ at 2% loading and 6.3 m² g⁻¹ at 10% loading. Furthermore, TEM analysis has been performed to obtain further insights into the structure and morphology of the dispersed MoS₂ phase. As shown in Fig. 4C and S7, the ZnS particles are predominantly covered by a shell

with a distinctive crystalline structure, consisting of an arrangement of 3 to 7 stacked planes extending longitudinally along the rounded support surface. In fact, the magnified image in Fig. 4D reveals that these planes are separated by approximately 0.6 nm, which is the characteristic interplanar spacing of (002) layers in the 2H-MoS₂ phase. These results suggest that MoS₂ interacts with the ZnS support preferentially through basal planes, possibly due to the shared S atoms and the similar hexagonal structures of 2H-MoS₂ and W-ZnS,³⁹ thus leading to the growth of thin and extensive MoS₂ layers in parallel to the ZnS surface, rather than in segregated MoS₂ particles. Such a morphology may be a key factor to explain the catalytic activity of 2% MoS₂/ZnS, as the exposed basal planes in few-layer MoS₂ are expected to provide active sites for CO₂ hydrogenation to methanol.⁵ Furthermore, the curved shape of the MoS₂ layers might also play a contributing role, as the presence of structurally strained layers has been previously associated with higher activity for methanol production.^{17,40}

In order to better understand the interaction between the active phase and the support in 2% MoS₂/ZnS, the catalyst has been compared with pure MoS₂ in an *in situ* XAS experiment under reaction-relevant conditions, consisting of a catalyst activation step at 300 °C under H₂ followed by exposure to a CO₂ + 3H₂ mixture at 200 °C. As expected, the H₂ pretreatment promotes the formation of sulfur vacancies with the release of H₂S, which has been detected for both samples *via* mass spectrometry, as shown in Fig. S8. During the subsequent step, no methanol has been detected as a reaction product, given that the experiment could only be performed with approximately 5 mg of catalyst at the pressure of 10 bar.

In the XANES spectra shown in Fig. 5A, the Mo K-edge of MoS₂ presents the typical features associated with the 2H-MoS₂ phase,⁴¹ and despite the detection of H₂S during the H₂ pretreatment, only negligible changes occur throughout the *in situ* experiment. This suggests that the formation of S-vacancies was not pronounced enough to elicit a deep structural modification detectable by XAS, but rather limited to the surface. In contrast with the high stability of bulk MoS₂, considerable differences are observed for 2% MoS₂/ZnS in Fig. 4B, as the

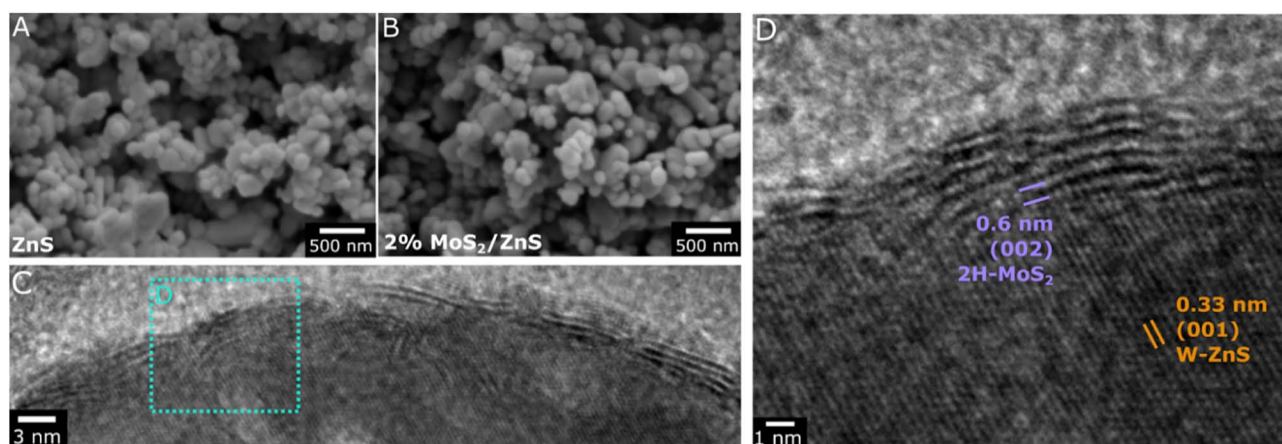


Fig. 4 SEM micrographs of ZnS before and after impregnation with 2% MoS₂ (A and B) and TEM images of 2%MoS₂/ZnS (C and D).



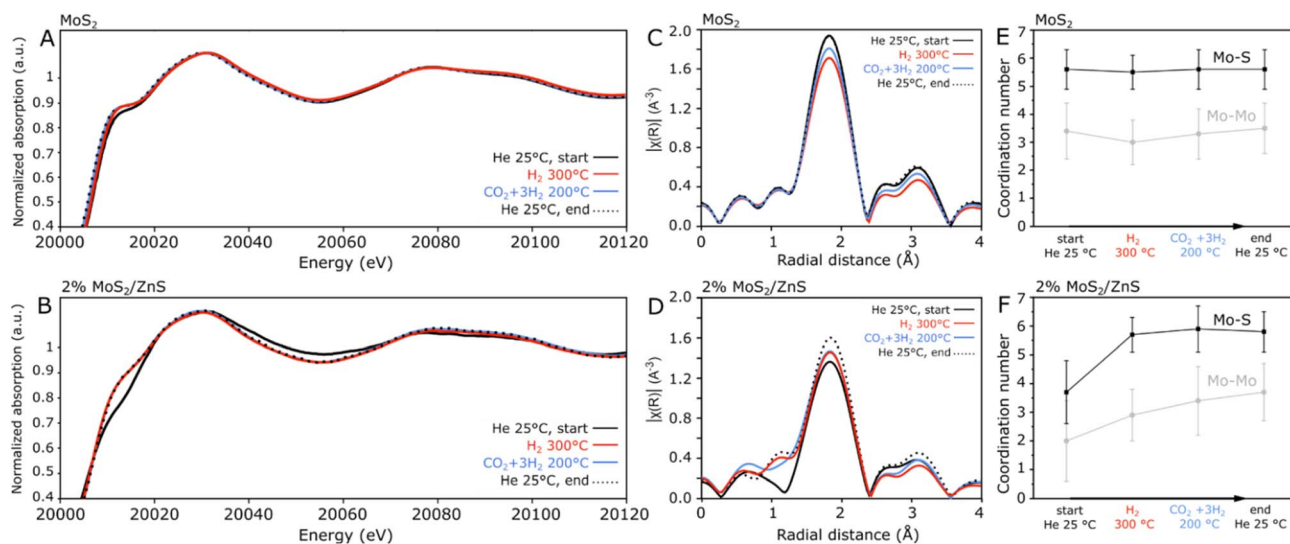


Fig. 5 *In situ* Mo K-edge XANES spectra with the respective EXAFS and EXAFS fitting summary for MoS₂ (A, C, E) and 2% MoS₂/ZnS (B, D, F), collected at 10 bar.

fresh catalyst has a considerably lower intensity in the 20 015 eV region. Furthermore, during the H₂ treatment, the spectrum undergoes considerable modification, and these changes persisted during reaction-like conditions and subsequent cooling to room temperature. In view of the XANES data, EXAFS analysis in Fig. 5C and D provides a more detailed description in terms of Mo–S and Mo–Mo coordination spheres, associated to the features at approximately 1.8 and 3.1 Å, respectively. While in pure MoS₂ the intensity changes of EXAFS profiles can be simply associated to sample temperature due to its effect on the Debye–Waller factor,⁴² 2% MoS₂/ZnS presents a more complex trend, with the H₂ treatment promoting a clear increase in the Mo–S peak rather than the decrease observed for MoS₂.

For a more comprehensive interpretation of such patterns, EXAFS fitting has been performed, using Mo–S and Mo–Mo paths of 2.41 and 3.15 Å, based on the 2H-MoS₂ reference (COD-1010993).⁴³ Considering the results presented in detail in Fig. S9 and Table S2, a summary of the fitted coordination numbers during the *in situ* experiment is shown in Fig. 5E and F. Although the ideal 2H-MoS₂ would show the same Mo–S and Mo–Mo coordination number of 6, the approximate values of 5.6 ± 0.7 and 3.4 ± 1.0 have been fitted for the bulk MoS₂ sample. The relatively low Mo–Mo coordination number can be associated with the limited crystallinity of the material,⁴¹ coherently with the broad reflections verified in XRD analysis. In line with the XANES and EXAFS results, merely negligible changes are visible in the MoS₂ fitting during the subsequent steps of the *in situ* experiment. On the other hand, a more pronounced difference is observed for 2% MoS₂/ZnS (Fig. 5F), with much lower initial coordination numbers of 3.7 ± 1.1 and 2.0 ± 1.4 for Mo–S and Mo–Mo, respectively. This suggests that in the as-synthesized material, highly defective MoS₂ interacts with the ZnS support, which rearranges following the H₂ treatment at 300 °C, as reflected by the clear increase in the Mo–S coordination, accompanied by an increment in Mo–Mo.

Following minor changes at reaction-similar conditions and cooling to room temperature, the spent 2% MoS₂/ZnS sample presents Mo–S and Mo–Mo coordination numbers comparable to those of pure MoS₂. Correspondingly with the XRD, XPS and SEM characterization, 10% MoS₂/ZnS shows XANES and EXAFS profiles seemingly in between those of 2% MoS₂/ZnS and MoS₂, as the material consists of a combination of bulk and ZnS-supported MoS₂.

According to the characterization of 2% MoS₂/ZnS, the initially defective MoS₂ shell is in close contact with the ZnS support, and the interaction between the sulfides promotes a partial restructuring of MoS₂ during the H₂ pretreatment, possibly due to filling of S-vacancies with sulfur derived from the ZnS support at the MoS₂/ZnS interface. Nevertheless, the increase in Mo–S coordination does not rule out the formation of sulfur vacancies at the catalyst surface, as simultaneous H₂S formation is verified by mass spectrometry as shown in Fig. S8. Furthermore, the few-layer character of the active phase is not altered during the H₂ pretreatment, as TEM analysis in Fig. S10 shows a similar morphology to the as-synthesized material.

With the observation of few-layer MoS₂ at the surface of ZnS and the subsequent catalytic activity for CO₂ hydrogenation to methanol, a comparison with a ZrO₂ reference support has been performed in order to better understand the influence of the support material on the active phase, given the typical application of ZrO₂ as a catalyst support for CO₂ hydrogenation.^{44,45} After the synthesis of 2% MoS₂/ZrO₂ by an analogous impregnation method, the formation of MoS₂ has been confirmed by the characteristic E_{2g} and A_{1g} vibrational bands in Raman spectroscopy and the prominent Mo⁴⁺ features in the XPS spectrum, as shown in Fig. S11. In a catalytic activity test at 200 °C summarized in Fig. 6A, 2% MoS₂/ZrO₂ exhibits a methanol yield corresponding to 70% of the value obtained for 2% MoS₂/ZnS, while methane production is doubled. Unlike the well-dispersed impregnation of MoS₂ on ZnS, SEM micrographs of



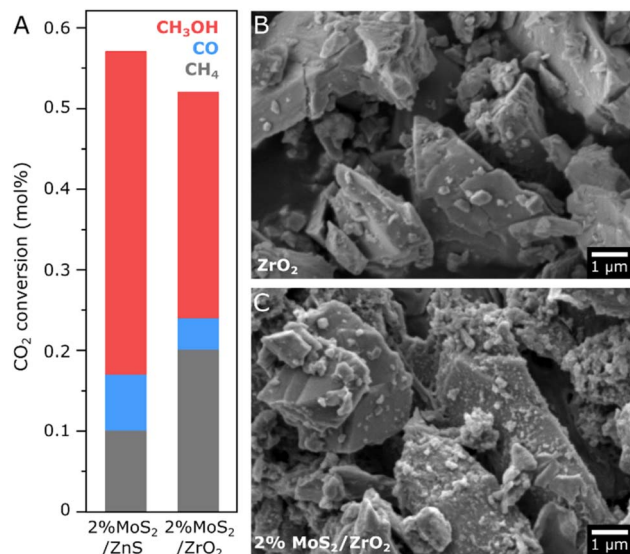


Fig. 6 Catalytic activity of 2% MoS₂/ZnS and 2% MoS₂/ZrO₂ at 20 bar/200 °C/0.25 g_{cat} in terms of CO₂ conversion to CH₄, CO and CH₃OH (A) and SEM micrographs of ZrO₂ before and after impregnation with 2% MoS₂ (B) and (C).

2% MoS₂/ZrO₂ in Fig. 6A and B show a much rougher surface morphology in comparison with the pure ZrO₂ support. Such a difference in dispersion suggests that the interaction of MoS₂ with the ZrO₂ surface does not favor homogeneous growth of a layered structure as in ZnS, thus leading to extensive agglomeration of MoS₂ in the form of nanoparticles with abundant edge sites, which may explain the less favorable selectivity for methanol production in comparison to the ZnS support. In accordance with the rougher morphology observed after impregnation, the BET surface area of 2% MoS₂/ZrO₂ is 3.7 m² g⁻¹, slightly higher than the pure support at 2.6 m² g⁻¹, while a similarly low porosity is verified in both N₂ isotherms. Furthermore, in view of recently reported carbon-based supports for highly active MoS₂ catalysts,⁴⁰ a 2% MoS₂/C catalyst has been additionally synthesized. In a preliminary comparison with 2% MoS₂/ZnS, the material presents a lower selectivity of about 34%, despite the doubled methanol yield, as shown in Fig. S12.

In order to better understand the interaction of CO₂ and H₂ with the surface of 2% MoS₂/ZnS in comparison with bulk and ZrO₂-supported MoS₂, temperature-programmed desorption (TPD) and reduction (TPR) experiments have been performed. In the CO₂-TPD results shown in Fig. S13, CO₂ is desorbed from bulk MoS₂ between 300 and 500 °C, indicating the presence of moderate to strong basic sites. Both 2% MoS₂/ZnS and 2% MoS₂/ZrO₂ show a less intense but similar desorption profile, which suggests similar basicity to bulk MoS₂. Despite such apparent similarity in CO₂ interaction, the samples exhibit considerable differences in H₂-TPR and H₂-TPD experiments, as shown in Fig. 7. In line with previous reports, Fig. 7A shows a sharp reduction feature for MoS₂ around 205 °C, associated with the release of H₂S and the simultaneous formation of sulfur vacancies. In the supported MoS₂ samples, this peak is

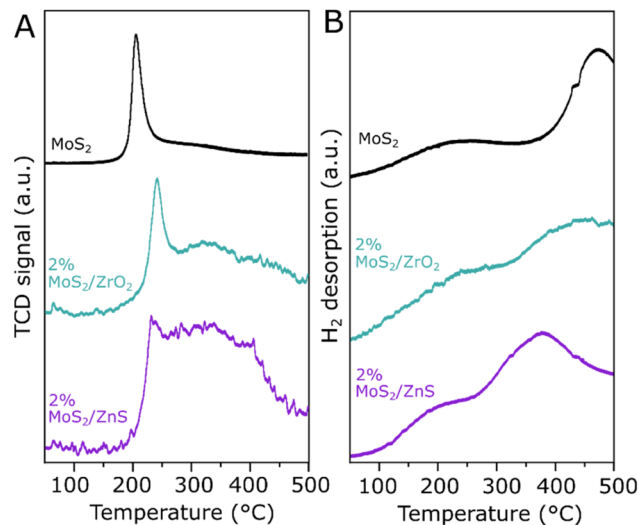


Fig. 7 H₂-TPR profiles after a 300 °C pretreatment in Ar (A) and H₂-TPD profiles after a 300 °C pretreatment in H₂ (B) for MoS₂, 2% MoS₂/ZrO₂ and 2% MoS₂/ZnS.

shifted to approximately 235 °C while a broader reduction feature arises in the range between 250 and 450 °C, the latter being particularly prominent for 2% MoS₂/ZnS. Considering that the pure ZrO₂ and ZnS supports do not show any significant reduction within the investigated temperature range, as shown in Fig. S13, this additional feature can be attributed to the MoS₂-support interface. Especially in 2% MoS₂/ZnS, the additional reduction feature above 250 °C may provide further evidence for the MoS₂/ZnS interaction suggested by *in situ* XAS experiment conducted under H₂ at 300 °C, as the dispersion of defective MoS₂ at the ZnS surface may help extracting S atoms from the support at the MoS₂/ZnS interface during catalyst pretreatment. In Fig. 7B, the H₂ desorption profile of MoS₂ shows two distinct features at approximately 220 °C and 475 °C. While the region at low temperature remains similar in the supported samples, the high-temperature H₂ desorption peak is shifted to 440 °C for 2% MoS₂/ZrO₂ and 375 °C for 2% MoS₂/ZnS. Such changes suggest that H₂ adsorbs less strongly on the supported MoS₂ catalysts than the bulk MoS₂. The trend correlates with the catalytic activity, where bulk-like MoS₂ converted more CO₂ to CH₄ than MeOH, suggesting that high surface coverage of hydrogen could promote such over-reduction.

To rationalize the support-dependent MoS₂ dispersion and restructuring observed experimentally, the interaction of pristine and sulfur vacant MoS₂ patches was studied in DFT simulations on the non-polar ZnS (100) and ZrO₂ (111) terminations, shown in Fig. S15, using thermodynamic metrics and the analysis of the projected density of states (PDOS).^{30,31,46} The patch model avoids the large artificial strain associated with constructing commensurate MoS₂ overlayers on the lattice-mismatched ZnS(100) and ZrO₂(111) surfaces, while capturing the local interfacial interactions. As shown by the optimized structural models in Fig. 8A and B, pristine MoS₂ is primarily stabilized through interactions at under-coordinated edge sites on both supports, although a qualitative difference emerges



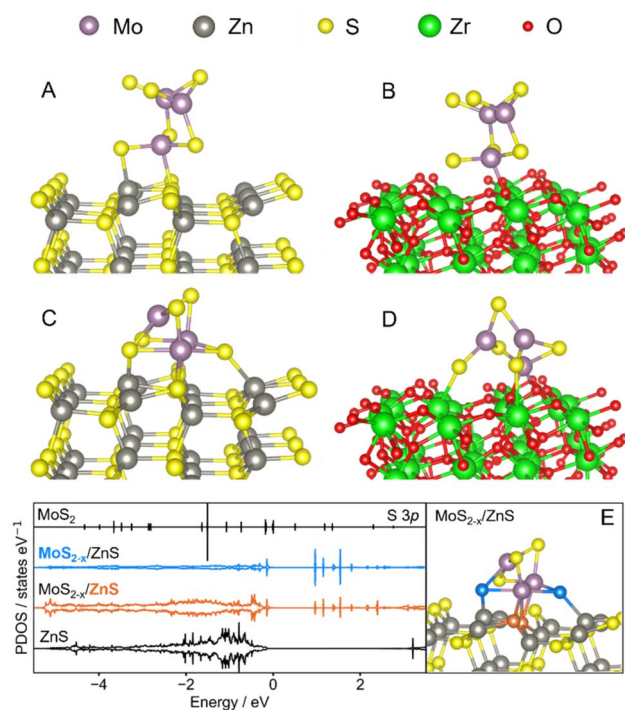


Fig. 8 Side view of the optimized interfaces: MoS₂/ZnS (A), MoS₂/ZrO₂ (B), MoS_{2-x}/ZnS (C), MoS_{2-x}/ZrO₂ (D) and MoS_{2-x}/ZnS interface highlighting the shared S atoms (coloured blue and orange) and their corresponding density of states projected on the S 3p states, together with MoS₂ and ZnS references (E).

upon formation of a sulfur vacancy. On ZnS, Fig. 8C shows that a reconstruction in which sulfurs are shared across the interface is the most stable configuration: sulfur atoms from ZnS coordinate to Mo edge sites while sulfur atoms originally belonging to MoS₂ bind to Zn. Interestingly, even in presence of an S-vacancy the characteristic geometry of the MoS₂ patch is retained at the interface with ZnS. This correlates with the favorable growth of homogeneous MoS₂ layers in close contact with the ZnS surface observed *via* TEM. Furthermore, such a pattern is not observed for the ZrO₂-based model in Fig. 8D, in which the MoS₂ patch becomes increasingly distorted due to the introduction of an S-vacancy, as sulfur sharing is not possible.

From a thermodynamic perspective, the relative energy penalty associated with the formation of a sulfur vacancy was evaluated consistently within each supported system, as the energy difference between the interacting pristine and defective MoS₂ systems normalized per MoS₂ unit, as shown in Table S3.⁴⁷ Despite the similar edge-mediated adsorption motifs observed for the pristine patch, sulfur-deficient MoS₂ configurations show a higher penalty for the removal of a sulfur on ZnS (1.47 eV) than on ZrO₂ (1.11 eV). This reflects the interfacial sharing occurring on the S-rich ZnS surface, which restores the coordination of MoS₂ through covalent Mo–S and Zn–S bonds perturbing the ZnS lattice.

The analysis of the PDOS (Fig. 8E) confirms the interfacial reconstruction from an electronic structure perspective. The PDOS fingerprint of the sulfur atoms shared across the MoS_{2-x}/

ZnS interface are remarkably similar due to the substantial overlap of their areas. In fact, the full-energy range Tanimoto similarity coefficient (T_C) was quantified as 0.410 (corresponding to an overlap fraction of $\sim 58\%$),³³ in contrast to the dissimilarity between sulfur atoms in isolated MoS₂ and ZnS ($T_C = 0.006$), reflecting intrinsically different electronic environments. Following the interfacial reconstruction, the sulfur atoms originating from MoS₂ undergo the highest electronic reconstruction, as evidenced by a T_C value of 0.002 with respect to the same atoms in isolated MoS₂. Conversely, the sulfur atoms originating from ZnS retain a significant degree of their electronic character ($T_C = 0.48$ with the corresponding atoms on isolated ZnS), while simultaneously rehybridizing at the interface. Overall, this indicates that the interfacial sulfur atoms exhibit a comparable hybridization and corroborates the formation of a shared sulfur electronic network at the MoS₂/ZnS interface, primarily driven by the reorganization of MoS₂, with ZnS acting as a sulfur-rich stabilizing environment that accommodates interfacial hybridization without fully losing its intrinsic electronic environment.

To further support this, the occupied centroids of the Mo 4d, S 3p and Zn 3d bands of MoS₂/ZnS, MoS_{2-x}/ZnS and ZnS were quantified. The changes in the states more involved in the interfacial bonding were highlighted by performing the analysis in proximity of the Fermi level, as shown in Fig. S16, focusing on the entire MoS₂ patch and the outermost layer of the ZnS (unit formula: 12 Zn and 12 S atoms).^{48,49} In agreement with the PDOS similarity analysis, the sulfur chemical potential of both MoS₂ and ZnS varied due to the reciprocal atoms sharing, as confirmed by the shift to higher energies of the S 2p states (from -0.95 to -0.72 eV for MoS₂ and from -1.07 to -0.95 eV for ZnS).⁴⁹ Accordingly, the Mo 3d band center of the patch shifts negatively (-0.51 eV to -0.75 eV), correlating with the increased Mo–S coordination,⁵⁰ and the Zn 3d states of ZnS shifts positively (from -1.04 to -0.91 eV), correlating with the sulfur-sharing and in agreement with the structural changes in the Zn sub-lattice following the reorganization required to reconstruct the vacant MoS₂ patch, shown in more detail in Fig. S17.⁵⁰

The DFT-based simulation results suggest that the ZnS support interacts with MoS₂ *via* sharing of sulfur atoms while keeping the integrity of the 2H-MoS₂ lattice. Such insights may explain the formation of few-layer MoS₂ on ZnS verified experimentally, in contrast with the agglomeration of MoS₂ observed at the surface of a ZrO₂ support. In view of these results, the sharing of sulfur atoms may be also closely related to the increase in the Mo–S coordination number observed in the *in situ* XAS experiment, as the formation of additional S-vacancies in MoS₂ may induce a bonding with sulfur from the MoS₂/ZnS interface during the H₂ pretreatment. While the dispersion of MoS₂ in the form of few layers is expected to be a key factor leading to catalytic CO₂ hydrogenation to methanol due to the likely presence of basal plane S-vacancies exposed at the surface, the potential role of the structural reconstruction verified during the H₂ pretreatment on catalytic activity still deserves further investigation.



Conclusions

In summary, this work demonstrates that MoS₂ can be supported on ZnS by means of a facile wet impregnation method, leading to enhanced catalytic activity for CO₂ hydrogenation to methanol in comparison with bulk MoS₂. Catalyst characterization in combination with DFT-based simulation suggest that such an improvement may be associated with the sulfur atom sharing and structural similarity at the MoS₂/ZnS interface, which help promote oriented growth of MoS₂ in the form of few layers with basal plane S-vacancies exposed at the surface, as these defects have been previously identified as active sites for methanol production from CO₂. In addition to this MoS₂/ZnS interaction, *in situ* XAS and H₂-TPR suggest that the H₂ pretreatment induces further interplay between the sulfides, as S-vacancy formation in MoS₂ promotes transfer of sulfur atoms from ZnS to MoS₂, possibly mediated by H₂S, thus leading to a partial reconstruction of the active phase. In contrast, when MoS₂ is impregnated onto the reference ZrO₂ support, the catalyst selectivity is considerably shifted towards methane, most likely in virtue of the more abundant edges in the MoS₂ particles, which are in this case more agglomerated at the support surface. Given the key role of MoS₂ morphology on CO₂ hydrogenation activity, these findings emphasize the importance of structural similarity in MoS₂-based composite catalysts, as this may be involved in the formation of a few-layer active phase on the ZnS support, and could also help explain other previous reports of a MoS₂/ZnS synergistic mechanism.¹⁴

Author contributions

Conceptualization: G. A. S. A. and K. F. Methodology: G. A. S. A., S. B., A. T. and K. F. Formal analysis: G. A. S. A. and S. B. Investigation: G. A. S. A., T. W., A. T., C. E., M. S. P. and D. C. C. B. Writing – original draft preparation: G. A. S. A. and S. B. Writing – review & editing: G. A. S. A., S. B., K. F., D. C. C. B., A. T. Supervision: K. F. Funding acquisition: K. F.

Conflicts of interest

There are no conflicts to declare.

Data availability

The data supporting this article have been included as part of the supplementary information (SI). Supplementary information is available. See DOI: <https://doi.org/10.1039/d6ta01545j>.

Acknowledgements

The authors thank the Diamond Light Source for beamtime (Proposal SP37966) and the staff of beamline B18, as well as Dr Davide Ferri from Paul Scherrer Institute, the CO₂ Refinery doctoral school, the Analytical Instrumentation Center (AIC), the X-ray Center (XRC) and the University Service Facility for Transmission Electron Microscopy (USTEM) at TU Wien. The computational results have been achieved using the Austrian

Scientific Computing (ASC) infrastructure. This project is funded by the FFG (<https://www.ffg.at/>) project CO2MethPro. The FFG is the central national funding agency and strengthens Austria's innovative capacity. This research was funded in part by the Austrian Science Fund (FWF) 10.55776/F8100. For open access purposes, the author has applied a CC BY public copyright license to any author accepted manuscript version arising from this submission.

References

- 1 P. Gabrielli, L. Rosa, M. Gazzani, R. Meys, A. Bardow, M. Mazzotti and G. Sansavini, *One Earth*, 2023, **6**, 682–704.
- 2 A. Álvarez, A. Bansode, A. Urakawa, A. V. Bavykina, T. A. Wezendonk, M. Makkee, J. Gascon and F. Kapteijn, *Chem. Rev.*, 2017, **117**, 9804–9838.
- 3 W. Gao, S. Liang, R. Wang, Q. Jiang, Y. Zhang, Q. Zheng, B. Xie, C. Y. Toe, X. Zhu, J. Wang, L. Huang, Y. Gao, Z. Wang, C. Jo, Q. Wang, L. Wang, Y. Liu, B. Louis, J. Scott, A.-C. Roger, R. Amal, H. He and S.-E. Park, *Chem. Soc. Rev.*, 2020, **49**, 8584–8686.
- 4 A. Beck, M. A. Newton, L. G. A. van de Water and J. A. van Bokhoven, *Chem. Rev.*, 2024, **124**, 4543–4678.
- 5 J. Hu, L. Yu, J. Deng, Y. Wang, K. Cheng, C. Ma, Q. Zhang, W. Wen, S. Yu, Y. Pan, J. Yang, H. Ma, F. Qi, Y. Wang, Y. Zheng, M. Chen, R. Huang, S. Zhang, Z. Zhao, J. Mao, X. Meng, Q. Ji, G. Hou, X. Han, X. Bao, Y. Wang and D. Deng, *Nat. Catal.*, 2021, **4**, 242–250.
- 6 A. M. Beale, E. K. Gibson, M. G. O'Brien, S. D. M. Jacques, R. J. Cernik, M. D. Michiel, P. D. Cobden, Ö. Pirgon-Galin, L. van de Water, M. J. Watson and B. M. Weckhuysen, *J. Catal.*, 2014, **314**, 94–100.
- 7 W. Torres, S. S. Pansare and J. G. Goodwin Jr, *Catal. Rev.:Sci. Eng.*, 2007, **49**, 407–456.
- 8 M. Vrinat, M. Breyse, C. Geantet, J. Ramirez and F. Massoth, *Catal. Lett.*, 1994, **26**, 25–35.
- 9 B. Han and Y. H. Hu, *Energy Sci. Eng.*, 2016, **4**, 285–304.
- 10 J. Sun and X. Meng, *ACS Appl. Nano Mater.*, 2021, **4**, 11413–11427.
- 11 L. A. Zavala-Sanchez, X. Portier, F. Maugé, L. Dubau and L. Oliviero, *Catal. Today*, 2025, **445**, 115020.
- 12 C. K. Poh, S. W. D. Ong, Y. Du, H. Kamata, K. S. C. Choong, J. Chang, Y. Izumi, K. Nariai, N. Mizukami, L. Chen and A. Borgna, *Catal. Today*, 2020, **342**, 21–31.
- 13 S. Zhou, W. Ma, M. Kosari, A. M. H. Lim, S. M. Kozlov and H. C. Zeng, *Appl. Catal., B*, 2024, **349**, 123870.
- 14 S. Zhou and H. C. Zeng, *ACS Catal.*, 2022, **12**, 9872–9886.
- 15 Z. Zhang, J. Zuo, L. Luo, X. Yang, Z. Ma, H. Jin, Y. Yuan, Q. Qian, Q. Chen and Y. Luo, *J. Catal.*, 2024, **436**, 115621.
- 16 M. Lin, M. Trubyanov, H. W. Lee, A. S. Ivanov, X. Zhou, P. Zhang, Y. Zhang, Q. Wang, G. S. X. Tan, K. S. Novoselov and D. V. Andreeva, *Small*, 2025, **21**, e2408592.
- 17 S. Zhou, W. Ma, U. Anjum, M. Kosari, S. Xi, S. M. Kozlov and H. C. Zeng, *Nat. Commun.*, 2023, **14**, 5872.
- 18 Y. Yuan, L. Qi, Z. Gao, T. Guo, D. Zhai, Y. He, J. Ma and Q. Guo, *Molecules*, 2023, **28**, 5796.



- 19 Z. Ma, Z. Zhang, Y. Chen, J. Su, J. Zuo, M. Yang, X. Wang, Q. Qian, Q. Chen and Y. Luo, *ACS Sustain. Chem. Eng.*, 2025, **13**, 10690–10700.
- 20 G. A. S. Alves, G. Pacholik, S. Pollitt, T. Wagner, R. Rameshan, C. Rameshan and K. Föttinger, *Catal. Sci. Technol.*, 2024, **14**, 1138–1147.
- 21 J. W. McDonald, G. D. Friesen, L. D. Rosenhein and W. E. Newton, *Inorg. Chim. Acta*, 1983, **72**, 205–210.
- 22 S. Gražulis, D. Chateigner, R. T. Downs, A. F. T. Yokochi, M. Quirós, L. Lutterotti, E. Manakova, J. Butkus, P. Moeck and A. Le Bail, *J. Appl. Crystallogr.*, 2009, **42**, 726–729.
- 23 N. Fairley, V. Fernandez, M. Richard-Plouet, C. Guillot-Deudon, J. Walton, E. Smith, D. Flahaut, M. Greiner, M. Biesinger, S. Tougaard, D. Morgan and J. Baltrusaitis, *Appl. Surf. Sci. Adv.*, 2021, **5**, 100112.
- 24 B. Ravel and M. Newville, *J. Synchrotron Radiat.*, 2005, **12**, 537–541.
- 25 G. Kresse and J. Furthmüller, *Comput. Mater. Sci.*, 1996, **6**, 15–50.
- 26 J. P. Perdew, K. Burke and M. Ernzerhof, *Phys. Rev. Lett.*, 1996, **77**, 3865–3868.
- 27 S. Bellomi, D. C. Cano-Blanco, I. Barlocco, J. J. Delgado, X. Chen, L. Prati, D. Ferri, N. Dimitratos, A. Roldan and A. Villa, *ACS Appl. Mater. Interfaces*, 2024, **16**, 54897–54906.
- 28 J.-X. Liu, Y. Su, I. A. W. Filot and E. J. M. Hensen, *J. Am. Chem. Soc.*, 2018, **140**, 4580–4587.
- 29 J. M. Wiesenfeld, J. Stone, D. Marcuse, C. A. Burrus and S. Yang, *J. Appl. Phys.*, 1987, **61**, 5447–5454.
- 30 E. Balantseva, G. Berlier, B. Camino, M. Lessio and A. M. Ferrari, *J. Phys. Chem. C*, 2014, **118**, 23853–23862.
- 31 C. Ricca, A. Ringuedé, M. Cassir, C. Adamo and F. Labat, *J. Comput. Chem.*, 2015, **36**, 9–21.
- 32 H. J. Monkhorst and J. D. Pack, *Phys. Rev.*, 1976, **13**, 5188–5192.
- 33 M. Kuban, S. Rigamonti, M. Scheidgen and C. Draxl, *Sci. Data*, 2022, **9**, 646.
- 34 P. Willett, J. M. Barnard and G. M. Downs, *J. Chem. Inf. Comput. Sci.*, 1998, **38**, 983–996.
- 35 S.-L. Li, H. Miyazaki, H. Song, H. Kuramochi, S. Nakaharai and K. Tsukagoshi, *ACS Nano*, 2012, **6**, 7381–7388.
- 36 J. H. Kim, H. Rho, J. Kim, Y.-J. Choi and J.-G. Park, *J. Raman Spectrosc.*, 2012, **43**, 906–910.
- 37 G. Deokar, D. Vignaud, R. Arenal, P. Louette and J.-F. Colomer, *Nanotechnology*, 2016, **27**, 075604.
- 38 P. Afanasiev and C. Lorentz, *J. Phys. Chem. C*, 2019, **123**, 7486–7494.
- 39 P. Hu, Z. Jia, Y. Wang, Q. Zhou, N. Liu, F. Li and J. Wang, *ACS Appl. Energy Mater.*, 2020, **3**, 7856–7864.
- 40 S. Zhou, M. Kosari and H. C. Zeng, *J. Am. Chem. Soc.*, 2024, **146**, 10032–10043.
- 41 L. Wu, A. Longo, N. Y. Dzade, A. Sharma, M. M. R. M. Hendrix, A. A. Bol, N. H. de Leeuw, E. J. M. Hensen and J. P. Hofmann, *ChemSusChem*, 2019, **12**, 4383–4389.
- 42 S. Caramazza, C. Marini, L. Simonelli, P. Dore and P. Postorino, *J. Phys.:Condens. Matter*, 2016, **28**, 325401.
- 43 R. G. Dickinson and L. Pauling, *J. Am. Chem. Soc.*, 1923, **45**, 1466–1471.
- 44 Y. Huang and Z. Duan, *J. Mater. Chem. A*, 2025, **13**, 4043–4089.
- 45 K. Li and J. G. Chen, *ACS Catal.*, 2019, **9**, 7840–7861.
- 46 Y. Li, C. Xu, D. Li, Y. Zhang, B. Liu and P. Huo, *Chem. Eng. J.*, 2024, **502**, 158151.
- 47 B. Kumela, R. Anvari and W. Wang, *J. Mater. Chem. C*, 2025, **13**, 22207–22216.
- 48 L. Qi, M. Che, M. Liu, B. Wang, N. Zhang, Y. Zou, X. Sun, Z. Shi, D. Li and S. Li, *Nanoscale*, 2023, **15**, 13252–13261.
- 49 X. Qiu, Y. Wang and Y. Jiang, *RSC Adv.*, 2020, **10**, 28725–28730.
- 50 F. Calle-Vallejo, *Adv. Sci.*, 2023, **10**, e2207644.

